Numerical Simulations of the Plasma Discharge in a Helicon Plasma Thruster

IEPC-2019-330

Presented at the 36th International Electric Propulsion Conference
University of Vienna, Austria
September 15-20, 2019

J. Zhou[*], P. Jiménez[†], M. Merino[‡], P. Fajardo[§] and E. Ahedo[¶]
Equipo de Propulsión Espacial y Plasmas, Universidad Carlos III de Madrid, Leganés 28911, Spain

Currently, the main problem for Helicon Plasma Thrusters (HPTs) is the lack of knowledge about its operation, and thus there are not proper guidelines for its design. In this paper, a novel 2D asymmetric code is proposed as a tool that could improve the understating of the physics behind and acts as a guidance that leads to a competitive design. This code fully models all the aspects of the plasma discharge. In the code, a hybrid approach is considered for the plasma production and transport: a fluid model is used for electrons and a Particle-In-Cell model for heavy species, which is a trade-off between computational feasibility and solution accuracy. As to the plasma-wave interaction, a frequency domain Finite Difference model based on a cold plasma is considered. The structure of the code and the integration of the different models are explained. The main difficulties in the development of this code are to find numerical algorithms that handle properly the low collisional and anisotropic electron fluid and the complex modelling of the plasma-wave interaction. The advances achieved in these difficulties are presented and discussed. After that, in order to show the capability of the code and its potential application as a guidance in real designs, this is used to run a simulation for a HPT thruster with a realistic configuration. From the simulation, 2D color maps of the discharge properties and thruster performances are obtained and studied. The study shows that the results are consistent physically and has allowed to propose improvements to its configuration.

I. Introduction

The Helicon Plasma Thruster (HPT) is a novel electric propulsion technology still in a research phase.[1–5] This technology is based on a helicon source to produce and heat the plasma, and a magnetic nozzle to generate thrust. Due to its characteristics, it has potential advantages: the lack of electrodes, thus reduced erosion problems and a longer lifetime; and the high throttlability due to the capability to act on the input power, the mass flow and the magnetic nozzle. However, the main drawback of this thruster is the poor performance, the current prototypes report thruster efficiency lower than 20%,[6,7] which are not competitive yet with the mature Hall Effect Thrusters (HET) and Gridded Ion Thrusters. One of the reasons for this low efficiency is that the physics behind HPT is not completely understood yet, which makes difficult its design.[8,9]

Our research group is developing a novel 2D axisymmetric code, HYPHEN. This code is aimed to be a multi-thruster simulation platform with applications for different electromagnetic thrusters, based on an externally applied stationary magnetic field to produce thrust by means of electromagnetic forces; and it is meant to solve self-consistently the complete plasma discharge. Its development started with HET,[10–13] and recently it has been improved, adapted and extended to HPT.[14,15] In a HPT there are two distinguished

[*]PhD Candidate, Aerospace Engineering Department, jzhou@pa.uc3m.es
[†]PhD Candidate, Aerospace Engineering Department, pejimene@ing.uc3m.es
[‡]Associate Professor, Aerospace Engineering Department, mario.merino@uc3m.es
[§]Associate Professor, Aerospace Engineering Department, pfajardo@ing.uc3m.es
[¶]Professor, Aerospace Engineering Department, eahedo@ing.uc3m.es

process in the discharge: (i) the plasma production and transport; and (ii) the plasma heating process via interaction with the radio-frequency waves, which is particular for these technologies and is not present in HET. The selected formulation for process (i), which has been inherited from the HET, is a hybrid one, consisting of a Particle-In-Cell (PIC) model for the heavy species and a fluid one for electrons. A remarkable feature of the electron formulation is the use of a Magnetic Field Aligned Mesh (MFAM) in order to handle its anisotropic character due to magnetization. For process (ii) an approach considering a cold plasma has been developed based on a Finite Difference model, and that works on the frequency domain.[16,17]

The paper is organized as follows. Section II describes the general structure of the code. Section III presents shortly the physical models implemented in the code and the numerical algorithms used to solve them. Section IV discusses the simulation results for a particular HPT thruster in order to show the capabilities of the code. Section V contains the conclusions.

II. Code Structure

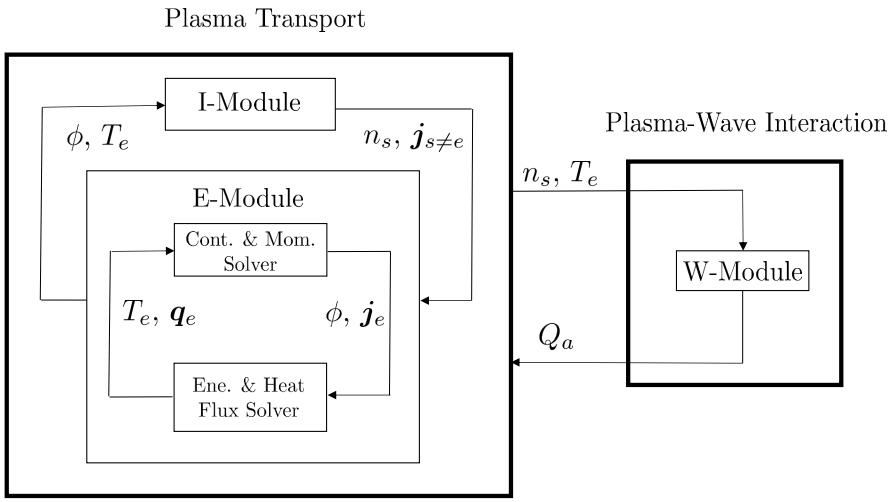

Figure 1. Scheme of code.

The code has three modules: an Ion(I)-module to compute the production and transport of the heavy species (ions and neutrals); an Electron(E)-module to solve the electron fluid; a quasi-neutral plasma is assumed, and for the non-neutral sheaths at the boundaries a Sheath(S)-module is used to solve them.[12,18] In case of HPT, an additional Wave(W)-module, which solves for the plasma-wave interaction, is added. The transport block integrates I-module, E-module and S-module and it is coded in FORTRAN; and the plasma-wave interaction block is just the W-module, which is coded in PYTHON. Both blocks are for now independent subcodes that are called from a PYTHON main script.

The integration of the modules for HPT is illustrated in Fig. 1:

- The plasma-wave interaction block (W-module) on the right takes as inputs the species densities and the electron temperature given by the transport block on the left (I-module and E-module). As output, it provides the deposited power density map. In the process, it computes also the wave-associated electric and magnetic fields.
- Inside the transport block, the I-module takes as inputs the electric potential and electron temperature from E-module to compute heavy species densities and currents. The E-module uses the outputs from the I-module and the W-module to compute its own outputs.
- Inside the E-module there are two solvers: one for continuity and momentum equations (solving for electric potential and electron currents) and another one for the energy and heat flux equations (solving for electron temperature and heat flux). These solvers are run separately in a sequential way each time E-module is called, i.e., one solver waits the other to finish to use its solutions as inputs.

In this scheme the S-module is not shown, it is coupled with E-module and allows to compute the electron properties and electric potential at the boundaries.

III. Physical Models/Numerical Treatment

The physical models and the numerical algorithms used are shortly discussed. We will focus only on the main difficulties of this code: the numerical treatment of the magnetized electron fluid in the E-module and the modelling of the plasma-wave interaction in the W-module. More details about other aspects of the code can be found in previous works.[11,12,14,15,18]

A. Plasma Transport

The fluid model for the electron transport is introduced. Recently, we have had advances in the numerical treatment of the electron continuity and momentum system.[15] The advances deal with algorithms that further reduces the numerical diffusion apart from the usage of a MFAM; and which improves the accuracy in the computation of the plasma properties at the boundaries, where a MFAM mesh present high irregularities. Now, these algorithms have been implemented for the energy and heat flux system. These improvements in the numerical resolution are presented here.

1. Current Continuity and Generalized Ohm's Law

The continuity and momentum system has been discussed in previous works[14,15] and it just briefly summarized here. Lets n_s, Z_s and $\boldsymbol{u}_s$ be the density, charge number and velocity of the species s respectively. The continuity equation for the electric current $\boldsymbol{j}$ is

$$\nabla \cdot \boldsymbol{j} = 0, \tag{1}$$

where $\boldsymbol{j} = \boldsymbol{j_i} + \boldsymbol{j_e}$, $\boldsymbol{j}_i = e\sum_{s\neq e} Z_s n_s \boldsymbol{u}_s$ is the ion current and $\boldsymbol{j}_e = -en_e\boldsymbol{u}_e$ the electron current. The electron momentum is modeled with a diffusive model, the electron inertia is neglected and the collisions are retained, and this allows to define a generalized Ohm's law. The Ohm's law projected in a reference frame defined by the applied magnetic field $\boldsymbol{B}_0$ yields

$$j_{\parallel e} = \sigma_e \left[\frac{1}{en_e}\frac{\partial\left(n_e T_e\right)}{\partial \mathbf{1}_\parallel} - \frac{\partial\phi}{\partial \mathbf{1}_\parallel}\right] - j_{\parallel c}, \tag{2}$$

$$j_{\perp e} = \frac{\sigma_e}{1+\chi^2}\left[\frac{1}{en_e}\frac{\partial\left(n_e T_e\right)}{\partial \mathbf{1}_\perp} - \frac{\partial\phi}{\partial \mathbf{1}_\perp}\right] - \frac{j_{\perp c} + j_{\theta c}\chi}{1+\chi^2}, \tag{3}$$

$$j_{\theta e} = -j_{\perp e}\chi - j_{\theta c}. \tag{4}$$

In these equations: $\mathbf{1}_\parallel$ and $\mathbf{1}_\perp$ are versors parallel and perpendicular (in the meridian plane) to $\boldsymbol{B}_0$ respectively, and θ represents the azimuthal direction; ϕ is the electric potential, T_e the electron temperature; $\sigma_e = e^2 n_e/(m_e\nu_e)$ is the current conductivity, with $\nu_e = \sum_{s\neq e}\nu_{es}$ the total electron collision frequency and which is obtained by adding the frequencies ν_{es} (dependent on n_s and T_e) with other species s; $\chi = \omega_{ce}/\nu_e$ is the Hall parameter, where $\omega_{ce} = eB_0/m_e$ is the electron gyrofrequency; and there are the components of $\boldsymbol{j}_c = en_e\sum_{s\neq e}\nu_{es}/\nu_e\boldsymbol{u}_s$, an equivalent current from the heavy species. Notice that, in Eq. (2) $\sigma_\parallel = \sigma_e$ is the parallel conductivity and in Eq. (4) $\sigma_\perp = \sigma_e/(1+\chi^2)$ is the perpendicular one, for magnetized electrons $\chi \gg 1$ and then $\sigma_\parallel \gg \sigma_\perp$ causing anisotropy.

In the parallel component of the Ohm's law, due to the low collisionality (thus, high conductivity $\sigma_e \propto \nu_e^{-1}$) of the plasma in electromagnetic thrusters, it happens that $(j_{\parallel e} + j_{\parallel c})/\sigma_e$ is small in the cases of interest[15] in Eq. (2) and the dominant terms are the pressure and potential gradients,

$$\frac{\partial\phi}{\partial \mathbf{1}_\parallel} \approx \frac{1}{en_e}\frac{\partial\left(n_e T_e\right)}{\partial \mathbf{1}_\parallel} \gg \frac{j_{\parallel e} + j_{\parallel c}}{\sigma_e}. \tag{5}$$

Then the equation is ill-conditioned numerically when trying to solve for $j_{\parallel e}$. The thermalized potential Φ, which groups the dominant terms, is proposed as a solution to this problem in Ref. 15. However, in that article a polytropic closure was assumed for T_e and the definition of Φ is relied on the existence of a barotropy

function. Under those conditions Φ is able to join totally the dominant terms in Eq. (2) as the gradient of Φ. However, the barotropy function does not exist for the general case, once T_e is obtained self-consistently with the energy equation. The definition of Φ proposed here for the general case is

$$\Phi = \phi - \frac{T_e}{e} \ln \frac{n_e}{n_{e0}}, \tag{6}$$

with n_{e0} as a reference density, and Eq. (2) becomes

$$j_{\parallel e} = \sigma_e \left[1/e \left(1 - \ln \frac{n_e}{n_{e0}} \right) \frac{\partial T_e}{\partial \boldsymbol{l}_\parallel} - \frac{\partial \Phi}{\partial \boldsymbol{l}_\parallel} \right] - j_{\parallel c}. \tag{7}$$

There is a term $\propto \partial T_e / \partial \boldsymbol{l}_\parallel$ remaining from pressure gradient, but it is known that also due to the low collisionality, T_e is nearly constant along $\boldsymbol{B}_0$ in electromagnetic thrusters,[8,19,20] and that term is of the same order as $(j_{\parallel e} + j_{\parallel c})/\sigma_e$.

In this system the continuity equation is a conservation law for $\boldsymbol{j}_e$ and the Ohm's law is a state equation that relates $\boldsymbol{j}_e$ and Φ. In order to solve this system, $\boldsymbol{j}_e$ from the Ohm's law is substituted in the conservation equation. First Φ is computed, and after that $\boldsymbol{j}_e$. The conservation equation is discretized and integrated in each cell with a Finite Volume Method (FVM). For the the Ohm's law, $\boldsymbol{j}_e$ is discretized at the cell face centers, their derivatives of Φ are set as a function of its discretized values at the cell centers through gradient reconstruction. In irregular meshes as a MFAM usually the Weight Least Square Method (WLSM), based on Taylor expansions, is one of the most extended methods to perform gradien reconstruction,[21,22] but it mixes the anisotropic properties between different directions to $\boldsymbol{B}_0$, which causes numerical diffusion. In Ref. 15 it is demonstrated that the better way to handle the derivatives of Φ is to use a Finite Difference Method (FDM). FDM is applied whenever possible, but it cannot be used for faces close to the contour due to the high irregularity of boundary cells, and WLSM is used there instead. In addition, as all the cell centers are inside the domain we need to complete the solution of Φ with its values the boundaries. For that a WLSM-based algorithm is applied in Ref. 15 and self-consistently values with the boundary conditions are obtained.

2. Energy conservation and Generalized Fourier's Law

The electron temperature (or pressure) and heat flux are obtained by solving the system composed of an energy conservation law and a closure equation for the heat flux. Regarding the energy conservation the classic internal energy equation is used. Then, for the heat flux a diffusive type model from Ref. 23, similar to the Ohm's law, is considered.

The internal energy equation is

$$\frac{\partial}{\partial t} \left(\frac{3}{2} n_e T_e \right) + \nabla \cdot \left(\frac{5}{2} n_e T_e \boldsymbol{u}_e + \boldsymbol{q}_e \right) = \boldsymbol{u}_e \cdot \nabla p_e + \sigma_e^{-1} \boldsymbol{j}_e \cdot (\boldsymbol{j}_e + \boldsymbol{j}_c) + Q_e - \frac{1}{2} m_e u_e^2 S_e + Q_a. \tag{8}$$

In this equation $\boldsymbol{q}_e$ is the heat flux, S_e the plasma production rate; Q_e contains the effects due to the inelastic collisions, whose contributions are

$$Q_e = Q_{ion} + Q_{exc}, \tag{9}$$

where Q_{ion} and Q_{exc} correspond to ionization and excitation, respectively; and Q_a is the power deposition that comes from plasma-wave interaction.

The model for $\boldsymbol{q}_e$ is

$$0 = -\frac{5 p_e}{2e} \nabla T_e - \boldsymbol{q}_e \times \boldsymbol{B} - \frac{5 p_e \sigma_e^{-1}}{2} (\boldsymbol{j}_e + \boldsymbol{j}_c) - e n_e \sigma_e^{-1} \boldsymbol{q}_e, \tag{10}$$

which is a generalized Fourier's law. Each of its component in the magnetic frame is given by

$$q_{\parallel e} = \frac{\sigma_e}{e n_e} \left[-\frac{5 p_e}{2e} \frac{\partial T_e}{\partial \boldsymbol{l}_\parallel} - \frac{5 p_e \sigma_e^{-1}}{2} \left(j_{\parallel e} + j_{\parallel c} \right) \right], \tag{11}$$

$$q_{\perp e} = \frac{\sigma_e / (e n_e)}{\chi^2 + 1} \left[-\frac{5 p_e}{2e} \frac{\partial T_e}{\partial \boldsymbol{l}_\perp} - \frac{5 p_e \sigma_e^{-1}}{2} \left(j_{\perp e} + j_{\perp c} \right) - \chi \frac{5 p_e \sigma_e^{-1}}{2} \left(j_{\theta e} + j_{\theta c} \right) \right], \tag{12}$$

and

$$q_{\theta e} = -\chi q_{\perp e} - \frac{5p_e}{2en_e}\left(j_{\theta e} + j_{\theta c}\right). \tag{13}$$

Here, lets take $k_\parallel = \sigma_e/(en_e)$ and $k_\perp = k_\parallel/(\chi^2+1)$ as the parallel and perpendicular heat conductivities respectively, notice that in a similar way as for current, here $k_\parallel \gg k_\perp$. Grouping all the terms this law can be written in a compact way as

$$\boldsymbol{q}_e = \overline{\overline{k}} \cdot \left[-\frac{5p_e}{2e}\nabla T_e - \frac{5p_e\sigma_e^{-1}}{2}\left(\boldsymbol{j}_e + \boldsymbol{j}_c\right)\right], \tag{14}$$

where $\overline{\overline{k}}$ is the heat conductivity tensor.

This system is analogous to the continuity and momentum one. The Fourier's law is also a state equation and the energy equation is a scalar conservation law but with a temporal character. Here, T_e is the equivalent to Φ and $\boldsymbol{q}_e$ to $\boldsymbol{j}_e$. Thus, in a similar way $\boldsymbol{q}_e$ is substituted in Eq. (8) with Eq. (14) to compute first T_e, once T_e is obtained the computation of $\boldsymbol{q}_e$ would be immediate. The algorithms used to solve this system is inherited from Ref. 15 ans is described below. The treatment of solution for the cells and for the boundaries are discussed separately.

Numerical Implementation-Inner Solution The temporal part of Eq. (8) is discretized with a semi-implicit Euler scheme of constant time step Δt. [In order to explain the numerical implementation, p_e is used instead of T_e to obtain more compact equations.] All the explicit p_e at its RHS is defined for the current time step $k+1$, except the nonlinear term in $\boldsymbol{q}_e$ from the temperature gradient, in that case the proportional p_e is taken at the previous time step k. This yields

$$\frac{3}{2}\frac{p_e|^{k+1} - p_e|^k}{\Delta t} = -\nabla\cdot\left(-\left.\frac{5p_e}{2en_e}\right|^{k+1}\boldsymbol{j}_e|^k + \boldsymbol{q}_e|^{k+1}\right) - \left.\frac{\boldsymbol{j}_e}{en_e}\right|^k \cdot \nabla p_e|^{k+1} + Q'_e|^k + Q_a|^k, \tag{15}$$

where

$$\boldsymbol{q}_e|^{k+1} = -\left(\frac{5p_e}{2e}\overline{\overline{k}}\right)^k \cdot \nabla\left(p_e/n_e\right)|^{k+1} - \left.\frac{5p_e}{2en_e}\right|^{k+1}\left(en_e\sigma_e^{-1}\right)\left|^k \overline{\overline{k}}\right|^k \cdot \left(\boldsymbol{j}_e + \boldsymbol{j}_c\right)|^k \tag{16}$$

and

$$Q'_e = \sigma_e^{-1}\boldsymbol{j}_e\cdot\left(\boldsymbol{j}_e + \boldsymbol{j}_c\right) + Q_e - \frac{1}{2}m_e\left(\frac{j_e}{en_e}\right)^2 S_e. \tag{17}$$

Then a FVM is applied to Eq. (15) for each cell l, it yields

$$\begin{aligned}\frac{3}{2}\frac{p_e|_l^{k+1} - p_e|_l^k}{\Delta t}V_l = &\sum_m \left(\left.\frac{5p_e}{2en_e}\right|^{k+1}\boldsymbol{j}_e|^k - \boldsymbol{q}_e|^{k+1}\right)\Bigg|_m S_m\cdot\boldsymbol{n}_m + \\ &+ \left(-\left.\frac{\boldsymbol{j}_e}{en_e}\right|^k \cdot \nabla p_e|^{k+1} + Q'_e|^k + Q_a|^k\right)\Bigg|_l V_l,\end{aligned} \tag{18}$$

V_l is the volume of the cell, m represent its faces, and S_m and $\boldsymbol{n}_m$ are the faces area and outward normal versor. For a contour face m^*, the known $\boldsymbol{q}_e\cdot\boldsymbol{n}|_{m^*}$ from boundary condition is imposed and the value from the step k is used to avoid the nonlinear relations from the sheath models at material walls.

In Eq. (18) the derivatives of p_e at a element l and face m are written in terms of its values at cell centers. Applying a gradient reconstruction method (GRM) it yields

$$\left.\frac{\partial p_e}{\partial \boldsymbol{l}}\right|_l = \sum_{l'} g_{ll'}\, p_e|_{l'} \tag{19}$$

and

$$\left.\frac{\partial p_e}{\partial \boldsymbol{l}}\right|_m = \sum_{l} g_{ml}\, p_e|_{l}\,. \tag{20}$$

Here $g_{ll'}$ and g_{ml} are geometric coefficients that depend only on the mesh, $\boldsymbol{l}$ a the unit vector for a generic direction and l' and l represent surrounding cells. In a similar way to Ref. 15 FDM is used in all the inner

faces except those close to the boundaries, where WLSM is applied. Regarding p_e at m an interpolation scheme is used obtaining

$$p_e|_m = \sum_l g'_{ml}\, p_e|_l\,, \tag{21}$$

which is only done for inner faces. Plugging these GRM and interpolation relations into Eq. (18), a linear system is obtained for $p_e|^{k+1}$ at the cells (number of equations equal to that of cells). However, the unknowns are $p_e|^{k+1}$ at the cells and boundary faces. Thus, additional equations for $p_e|^{k+1}_{m^*}$ are needed.

Numerical Implementation-Boundary Solution The boundary algorithm for Φ in Ref. 15 is applied for p_e. In this algorithm, a WLSM is introduced, which for a boundary face m^* includes $p_e|_{m^*}$ (apart from $p_e|_l$) as well and it has the form

$$\left.\frac{\partial p_e}{\partial \boldsymbol{l}}\right|_{m^*} = \sum_l g_{m^*l}\, p_e|_l + g_{m^*}\, p_e|_{m^*}\,. \tag{22}$$

Then the electron heat flux from Eq. (16) at face m^* is forced to be equal to the value given by the boundary condition, it yields

$$\begin{aligned}&\frac{5}{2e}\left[p_e|^k_{m^*}\, g_{m^*} + (en_e\sigma_e^{-1})\big|^k_{m^*}\, (\boldsymbol{j}_e+\boldsymbol{j}_c)|^k_{m^*}\cdot\boldsymbol{n}'_{m^*}\right]\left.\frac{p_e}{n_e}\right|^{k+1}_{m^*} + \frac{5}{2e}\, p_e|^k_{m^*}\sum_l g_{m^*l}\left.\frac{p_e}{n_e}\right|^{k+1}_{l} = \\ &\frac{-\,(\boldsymbol{q}_e\cdot\boldsymbol{n})|^k_{m^*}}{|\,\overline{\overline{k}}^T\Big|^k_{m^*}\cdot\boldsymbol{n}_{m^*}|},\end{aligned} \tag{23}$$

where

$$\boldsymbol{n}'_{m^*} = \frac{\overline{\overline{k}}^T\Big|^k_{m^*}\cdot\boldsymbol{n}_{m^*}}{|\,\overline{\overline{k}}^T\Big|^k_{m^*}\cdot\boldsymbol{n}_{m^*}|}, \tag{24}$$

Equation (22) has been introduced, and the GRM coefficients g_{m^*} and g_{m^*l} are for the derivative along $\boldsymbol{n}'_m$. Concatenating the equation for each boundary face we obtain a linear system for $p_e|^{k+1}_{m^*}$.

Numerical Implementation-Complete System The system in Eq. (18) has to solved together with Eq. (23), grouping them the final system has the form

$$A\begin{bmatrix}\{p_e|^{k+1}_l\}\\ \{p_e|^{k+1}_{m^*}\}\end{bmatrix} = \boldsymbol{b}, \tag{25}$$

where A contains the physical and geometric coefficients proportional to $p_e|^{k+1}$ and $\boldsymbol{b}$ groups the terms at step k and the boundary condition for $\boldsymbol{q}_e$.

B. Plasma-Wave Interaction

The following full-wave Finite Difference method is based on the model of Tian[17] for the study of electromagnetic wave propagation in cold plasmas. The mathematical model, numerical implementation and application for the simulation of a Helicon thruster are presented.

1. Wave propagation model

Fourier analysis is used to obtain the frequency domain form of Maxwell's equations. The time-harmonic electric field vector for a monochromatic wave with a given excitation angular frequency ω is shown in Eq. (26). Note that the term $\hat{\boldsymbol{E}}$ multiplying the exponential factor is a complex amplitude containing information both about the magnitude and phase of the time varying field. The electric and magnetic fields and the current density vector can be expressed in complex exponential form, not only in time but in space as well.

By virtue of linearity, the solution to a full electromagnetic propagation problem with an excitation frequency ω and different azimuthal modes m is the superposition of many terms of the form

$$\boldsymbol{E}(\boldsymbol{r},t) = \Re[\hat{\boldsymbol{E}}(\boldsymbol{r},\omega)\exp(-i\omega t)] = \Re[\tilde{\boldsymbol{E}}(z,r,m,\omega)\exp(-i\omega t + im\theta)]. \tag{26}$$

Projecting into cylindrical coordinates with r denoting the radial direction and z the axial coordinate, the spatial dependence has been reduced by such expansion in the azimuthal direction θ. Field continuity is imposed by satisfying the condition that the azimuthal wave number belongs to the set of integer numbers $m \in \mathbb{Z}$.

In order to discretize Maxwell equations into the grid shown in Fig. 3, it is helpful to use the first order form of Faraday's and Ampere's laws in integral form,

$$\begin{aligned} \omega \textstyle\int i\tilde{\boldsymbol{B}}\cdot \mathrm{d}s - \oint \tilde{\boldsymbol{E}}\cdot \mathrm{d}l = 0 \\ \mu_0\omega \textstyle\int i\tilde{\boldsymbol{D}}\cdot \mathrm{d}s + \oint \tilde{\boldsymbol{B}}\cdot \mathrm{d}l = \mu_0 \textstyle\int \tilde{\boldsymbol{j}}_a\cdot \mathrm{d}s \end{aligned} \tag{27}$$

where ε_0 and μ_0 are the vacuum permittivity and permeability; and $c = \sqrt{1/(\varepsilon_0\mu_0)}$ is the speed of light in vacuum. The displacement field $\tilde{\boldsymbol{D}} = \varepsilon_0\bar{\bar{\kappa}}\cdot\tilde{\boldsymbol{E}}$ is introduced as the 'effective' propagating field within certain material and matches the electric field in vacuum. The dielectric tensor $\bar{\bar{\kappa}}$ can be derived from the plasma current for a cold and magnetized plasma.[24] Notice that the effect of the plasma current has been included in the dielectric tensor and only the antenna current density $\tilde{\boldsymbol{j}}_a$ appears explicitly in the expression (the total current is $\tilde{\boldsymbol{j}}_p + \tilde{\boldsymbol{j}}_a$).

The expression found in Eq. (27) relies on the fact that, neglecting thermal motion in the momentum equation for each species s in the plasma and under the influence of an externally applied magnetic field $\boldsymbol{B}_0$ (different from the wave magnetic field), it is possible to find a linear relation between the species current density and the electric field,

$$\tilde{\boldsymbol{j}}_s = \bar{\bar{\sigma}}_s\cdot\tilde{\boldsymbol{E}}, \tag{28}$$

where $\bar{\bar{\sigma}}_s$ is the conductivity tensor for s. After which $\bar{\bar{\kappa}}$ is derived as

$$\bar{\bar{\kappa}}(\omega) = \bar{\bar{1}} + \sum_s \frac{i}{\omega\varepsilon_0}\bar{\bar{\sigma}}_s. \tag{29}$$

Selecting a Cartesian coordinate system with the static magnetic field directed along the z-direction $\boldsymbol{B_0} = B_0\mathbf{1_z}$, the dielectric tensor takes the form[24]

$$\bar{\bar{\kappa}} = \begin{pmatrix} S & -iD & 0 \\ iD & S & 0 \\ 0 & 0 & P \end{pmatrix} \tag{30}$$

with:

$$S \equiv \frac{1}{2}(R+L) \tag{31}$$

$$D \equiv \frac{1}{2}(R-L) \tag{32}$$

$$P \equiv 1 - \sum_s \frac{\omega_{ps}^2}{\omega(\omega + i\nu_m)} \tag{33}$$

$$R \equiv 1 + \sum_s \chi_s^- = 1 - \sum_s \frac{\omega_{ps}^2}{\omega(\omega + i\nu_m + \omega_{cs})} \tag{34}$$

$$L \equiv 1 + \sum_s \chi_s^+ = 1 - \sum_s \frac{\omega_{ps}^2}{\omega(\omega + i\nu_m - \omega_{cs})} \tag{35}$$

and:

$$\omega_{cs} = \frac{Z_s e B_0}{m_s}, \qquad \omega_{ps}^2 = \frac{n_s(Z_s e)^2}{m_s\varepsilon_0}. \tag{36}$$

In these expressions ω_{cs} is the species cyclotron frequency, ω_{ps} is the plasma frequency, and m_s is the particle's mass. Finally, ν_m is the effective momentum loss frequency due to collisions.

To close the problem, a suitable set of boundary conditions must be enforced. For metallic walls Perfect Electric Conductor (PEC) BCs are applied in all the boundaries besides the axis by imposing a null tangential field $\tilde{\boldsymbol{E}} \times \boldsymbol{n} = 0$. The staggered grid in Fig. 3 provides an easy implementation because the tangential fields lay precisely on the boundaries and, thus, the condition can be simply included as additional equations in the fully discretized system. When it comes to the axis, the application of BCs turns out to be more convoluted. The following conditions should be met to prevent the fields going to infinity and ensure continuity[25] (similar expressions are found for $\boldsymbol{B}$),

$$\begin{aligned} \tilde{E}_r^{(0)} &= \tilde{E}_\theta^{(0)} = 0, \\ \tilde{E}_r^{(\pm 1)} &= \mp i \tilde{E}_\theta^{(\pm 1)}, \quad \tilde{E}_z^{(\pm 1)} = 0, \\ \tilde{E}_r^{(m)} &= \tilde{E}_\theta^{(m)} = \tilde{E}_z^{(m)} = 0 \quad |m| > 1. \end{aligned} \tag{37}$$

2. Antenna modelling

Helical antennas have proven to deliver a good performance in terms of power deposition into the plasma.[26] This section is devoted to the modelling of those antennas for their application in the wave module.

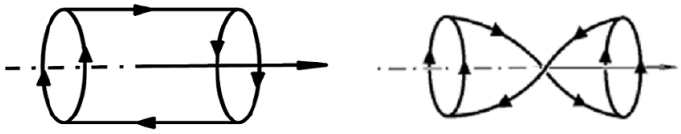

Figure 2. Nagoya III and half turn helical antenna[27,28]

For an antenna of length l_a, centered around r_a and having $h \in \mathbb{R}$ turns per loop, the ratio of axial to total current in the central helix is $[(2\pi hr/l_a)^2 + 1]^{-1/2}$. The water-bag function is defined to truncate the antenna in the axial direction,

$$G\left(z; z_1, z_2\right) = H\left(z - z_1\right) - H\left(z - z_2\right) = \begin{cases} 1, & z_1 < z < z_2 \\ 0, & \text{otherwise} \end{cases}, \tag{38}$$

where $H(z - z_0)$ is the Heaviside unit step function and z_1 and z_2 are the axial coordinates of the antenna ends. Using the above equations, the following expression can be found for the axial current density in any antenna of the helical family

$$j_{za}(z, r, \theta) = \frac{I_a F(r)}{r\sqrt{(2\pi hr/l_a)^2 + 1}} G(z; z_1, z_2) \left(\delta(\theta - \frac{2\pi h[z - z_1]}{l_a}) - \delta(\theta - \pi - \frac{2\pi h[z - z_2]}{l_a}) \right). \tag{39}$$

In the azimuthal direction, besides the central helix, the two lateral loops must be added

$$\begin{aligned} j_{\theta a}(z, r, \theta) = I_a F(r) \Bigg[& G(z; z_1, z_2) \frac{2\pi h}{l_a \sqrt{(2\pi hr/l_a)^2 + 1}} \left(\delta(\theta - \tfrac{2\pi h[z - z_1]}{l_a}) - \delta(\theta - \pi - \tfrac{2\pi h[z - z_2]}{l_a}) \right) + \\ & + \tfrac{1}{2} \delta\left(z - z_1\right) \left[G(\theta; 0, \pi) - G(\theta; \pi, 2\pi) \right] \\ & - \tfrac{1}{2} \delta(z - z_2) [G(\theta; 2\pi h, 2\pi h + \pi) - G(\theta; 2\pi h + \pi, 2\pi h + 2\pi)] \Bigg], \end{aligned} \tag{40}$$

such that $\int_0^{r_w} F(r) dr = 1$, with r_w being the maximum radius of the rectangular domain. This function is used to smooth the profile in the radial direction either for numerical reasons or to simulate an antenna of

some characteristic thickness d_t, for an infinitely fine antenna we have $F(r) = \delta(r - r_a)$. For the implementation into the 2D axisymmetric code, it is neccesary to perform an expansion in Fourier series along the θ direction

$$f(\theta) = \sum_{m=-\infty}^{\infty} f^{(m)} e^{im\theta}, \qquad f^{(m)} = \frac{1}{2\pi} \int_0^{2\pi} f(\theta) e^{-im\theta} d\theta. \tag{41}$$

The Fourier components are

$$j_{za}^{(m)}(z,r) = \frac{I_a F(r)(1 - e^{-im\pi})}{r\sqrt{(2\pi hr/l_a)^2 + 1}} \left[G(z; z_1, z_2) \frac{e^{-2im\pi h[z-z_1]/l_a}}{2\pi} \right], \tag{42}$$

$$j_{\theta a}^{(m)}(z,r) = I_a F(r)(1 - e^{-im\pi}) \left[G(z; z_1, z_2) \frac{h e^{-2im\pi h[z-z_1]/l_a}}{l_a\sqrt{(2\pi hr/l_a)^2 + 1}} - \frac{1}{2\pi}\delta(z - z_1) + \frac{1}{2\pi}\delta(z - z_2)\, e^{-2imh\pi} \right]. \tag{43}$$

Notice that, due to the presence of $(1 - e^{-im\pi})$, the current vanishes for even modes while it doubles for odd m.

In the case of a Nagoya III antenna,[17] which is used below for a simulation case, the axial current density in Eq. (42) simplifies with h=0 yielding

$$\begin{gathered} j_{za}^{(m)}(z,r) = \frac{I_a}{\pi r} G(z; z_1, z_2) F(r) \\ \text{if } m \text{ odd} \ ; \quad j_z = 0 \text{ otherwise,} \end{gathered} \tag{44}$$

where a normalized Gaussian function is used to smooth the r profile, and taking d_t as the characteristic thickness of the wire one has

$$\begin{gathered} F(r) = w^{-1} \exp\left(-\tfrac{(r-r_a)^2}{d_t^2}\right) \\ \text{with } w = \int_0^{r_w} \exp\left(-\tfrac{(r-r_a)^2}{d_t^2}\right) dr = \tfrac{1}{2}\sqrt{\pi} d_t \left[\operatorname{erf}\left(\tfrac{r_a}{d_t}\right) - \operatorname{erf}\left(\tfrac{r_a - r_w}{d_t}\right) \right]. \end{gathered} \tag{45}$$

The azimuthal current density is derived from the axial profile so as to satisfy conservation of charge $\nabla \cdot \boldsymbol{j}_a = 0$, taking $j_{ra}^{(m)} = 0$ this reads

$$j_{\theta a}^{(m)} = i \frac{r}{m} \frac{\partial j_{za}^{(m)}}{\partial z}. \tag{46}$$

Previous work[26] has shown that the mode $m = 1$ accounts for up to 98% of the plasma resistivity when using Nagoya III antenna. Therefore, the simulation of the next section is run only for this particular azimuthal mode.

3. Numerical implementation

The numerical solution of the wave problem is obtained using a Finite Difference method, in particular, a modification of the well-known Yee staggered grid method to account for non-isotropic linear materials such as a cold magnetized plasma. Unlike the original leapfrog time marching Yee method, Maxwell's equations are solved in the frequency domain on account of the shortest wave propagation characteristic time when compared to the electron thermal velocity in the transport problem.

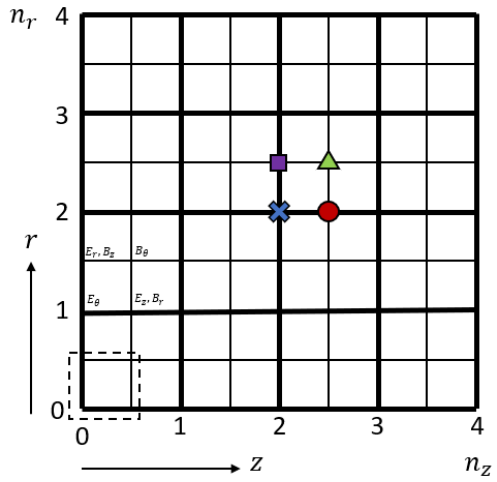

Figure 3. 2D staggered grid and electromagnetic fields. Each cell comprises a central node and four border nodes. E_θ is located in the blue X, E_z and B_r in the red circle, E_r and B_z in the purple square and finally B_θ in the green triangle.

The use of the staggered grid with alternating fields for the nodes inside a cell allows for an easy implementation of the surface and line integrals. The difference in the discretization with the vacuum Yee method arises from the need to estimate the value of the electric field in certain nodes where it is not solved for in the assembled system of equations. This requirement comes from the dielectric tensor times electric field product in the computation of the displacement field. A straightforward solution is to perform simple interpolations using nearby nodes where the electric field unknowns are placed. By discretizing Eq. (27) into the grid shown in Fig. 3, Eqs. (47) and (48) are found for each cell (i_z, i_r) in the domain as

$$\begin{aligned}
i\omega\rho B_z\left(i_z,i_r\right)dr + imE_r\left(i_z,i_r\right)dr - \rho E_\theta\left(i_z,i_r+1\right) + \rho E_\theta\left(i_z,i_r\right) = 0\\
i\omega\rho B_r\left(i_z,i_r\right)dz - imE_z\left(i_z,i_r\right)dz + \rho E_\theta\left(i_z+1,i_r\right) - \rho E_\theta\left(i_z,i_r\right) = 0\\
i\omega B_\theta\left(i_z,i_r\right)dzdr - E_z\left(i_z,i_r\right)dz - E_r\left(i_z+1,i_r\right)dr + E_z\left(i_z,i_r+1\right)dz + E_r\left(i_z,i_r\right)dr = 0,
\end{aligned} \tag{47}$$

$$\begin{aligned}
\tfrac{\omega}{c^2}\left[i\rho\kappa_{zr}\tfrac{E_r(i_z,i_r)+E_r(i_z+1,i_r)+E_r(i_z+1,i_r-1)+E_r(i_z,i_r-1)}{4} + i\rho\kappa_{r\theta}\tfrac{E_\theta(i_z+1,i_r)+E_\theta(i_z,i_r)}{2} + i\rho\kappa_{zz}E_z\left(i_z,i_r\right)\right]\Delta r\\
-imB_r\left(i_z,i_r\right)\Delta r - \rho B_\theta\left(i_z,i_r-1\right) + \rho B_\theta\left(i_z,i_r\right) = \mu_0\rho j_{ar}\Delta r
\end{aligned}$$

$$\begin{aligned}
\tfrac{\omega}{c^2}\left[i\rho r_{rr}E_r\left(i_z,i_r\right) + i\rho\kappa_{r\theta}\tfrac{E_\theta(i_z,i_r+1)+E_\theta(i_z,i_r)}{2} + i\rho\kappa_{rz}\tfrac{E_z(i_z,i_r)+E_z(i_z-1,i_r)+E_z(i_z-1,i_r+1)+E_z(i_z,i_r+1)}{4}\right]\Delta z\\
+imB_z\left(i_z,i_r\right)\Delta z + \rho B_\theta\left(i_z-1,i_r\right) - \rho B_\theta\left(i_z,i_r\right) = \mu_0\rho j_{ar}\Delta z
\end{aligned}$$

$$\begin{aligned}
\tfrac{\omega}{c^2}\left[i\kappa_{\theta r}\tfrac{E_r(i_z,i_r)+E_r(i_z,i_r-1)}{2} + i\kappa_{\theta\theta}E_\theta\left(i_z,i_r\right) + i\kappa_{\theta z}\tfrac{E_z(i_z,i_r)+E_z(i_z-1,i_r)}{2}\right]\Delta z\Delta r\\
-B_z\left(i_z,i_r\right)\Delta z + B_z\left(i_z,i_r-1\right)\Delta z + B_r\left(i_z,i_r\right)\Delta r - B_r\left(i_z-1,i_r\right)\Delta r = \mu_0 j_{a\theta}\Delta z\Delta r.
\end{aligned} \tag{48}$$

The tildes have been dropped for simplicity in the notation. ρ denotes the radial coordinate r of the central node for the cell (i_z, i_r) and Δr and Δz are the cell sides' lengths. The set of $6 \times n_z \times n_r$ equations (including boundary conditions) is assembled into the usual linear system form $A\boldsymbol{x} = \boldsymbol{b}$, where A is the matrix of coefficients and $\boldsymbol{b}$ is the forcing vector (antenna currents). A direct solver is applied to obtain the electric and magnetic field components contained in the solution vector $\boldsymbol{x}$. Averaging during a whole wave cycle $T = 2\pi/\omega$, the power deposited into the plasma reads $Q_a = \Re\left(\dfrac{\boldsymbol{j}_p^* \cdot \boldsymbol{E}}{2}\right)$, then the total power absorption can be computed as

$$P_a = \Re\left(\int_{V_p} \frac{\boldsymbol{j}_p^* \cdot \boldsymbol{E}}{2} \mathrm{d}V_p\right), \tag{49}$$

being V_p the volume comprising the plasma region.

IV. Results

A. Simulation Set-up

The code is used to run a simulation for a HPT thruster sketched in Fig. 4, which is similar in configuration to the prototype HPT05.[5,6] The summary of the settings can be found in Table 1. The thruster has a vessel with a length l_c=13cm and radius r_c=1cm. The walls are made of ceramic material (W2) and there is an injector at the back surface (W1), which starts from r=0cm and has an extension of r_{inj}=0.2cm and delivers Xenon at a mass flow rate of $\dot{m}$ =1mg/s. From z=13cm we have the truncated plume with a free loss surface (W3). The illustrated magnetic field is generated with a coil, which works as the magnetic nozzle in the plume. The antenna shown is a Nagoya III,[17] with a radius r_a=1.2cm, length l_a=7.5cm, thickness d_t=0.05cm and a central position z_a=5.25cm. The antenna operates at f=50MHz and its current is adjusted to have a constant total power deposited to the plasma of P_a=300W.

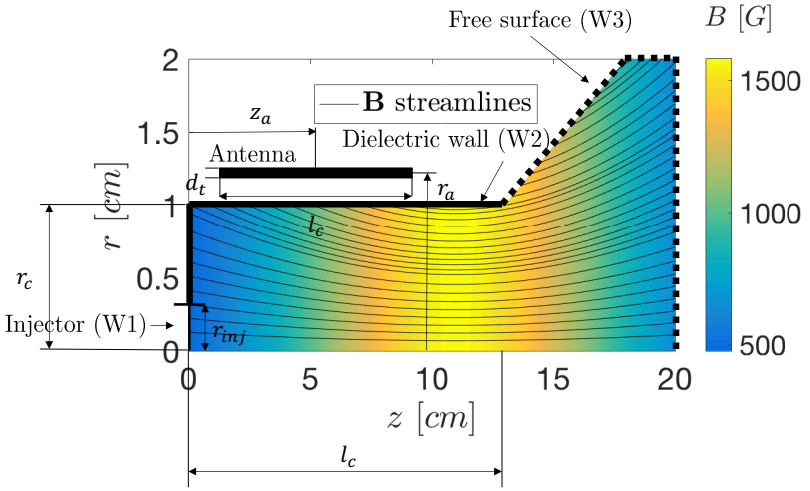

Figure 4. Scheme of the HPT thruster simulated.

Regarding the BCs, some of the BCs for the W-module do not exactly match those used for the transport. The dielectric material of the HPT source has a small effect on the fields propagation and it is ignored for the present simulations. Moreover, the wavelength in vacuum is several meters long, plasma currents are excited inductively and distinguishable waves only develop inside the plasma region. Additionally, the truncation of the domain is carried out using Perfect Electric Conductor (PEC) BCs (except for the axis) accounting for metallic walls. This is a good first approximation to the actual laboratory case taking into account that, inside the vacuum chamber, there is not actual free space radiation.

B. Discharge 2D Profiles

Figure 5 shows the 2D maps for properties in the plasma discharge. Subplots (a), (b), (c), (d), (e), (f), (h) and (i) are the solutions from the transport block while (g), (j), (k) and (l) are from the W-module.

Studying the results it is found that:

- The plasma density [subplot (b)] presents a maximum on the axis and around $z_{n_{max}}$=3.2cm. Then it decays due to plasma recombination at the walls and expansion in the plume. The large magnetic field around z=13cm (B_0 about 1500G) makes n_e to decay nearly 2 order of magnitude and a good

Parameter	
Chamber length l_c	13 cm
Chamber radius r_c	1 cm
Mass flow $\dot{m}$	1mg/s
Propellant type	Xenon
Antenna type	Nagoya III
Antenna frequency f	50 MHz
Antenna loop radius r_a	1.2 cm
Antenna length l_a	7.5 cm
Antenna central position z_a	5.25 cm
Antenna thickness d_t	0.05 cm
Power deposition P_a	300 W

Table 1. Simulation Parameters

confinement is achieved in that region. However, the problem is upstream from z=0cm to $z_{n_{max}}$, where B_0 has decay 2-3 times (from 1500G) and n_e is practically of same order as its maximum value.

- Subplot (c) is the neutral density, the depletion of neutrals due to ionization can be observed. Besides, at the plume it reaches much lower magnitudes ($10^{16}/m^3$) compared with the plasma ($10^{18}/m^3$), which means that nearly all the injected propellant is ionized.

- Subplot (e) is the ion longitudinal current density. [The longitudinal current density of a species s is defined as $\boldsymbol{j}_s^{'} = \boldsymbol{j}_s - j_{\theta s}\boldsymbol{l}_\theta$.] From its analysis, conclusions consistent with those from n_e are obtained. The streamlines are born from the axial position of maximum n_e. There are virtually no ions going to the lateral wall for $z > z_{n_{max}}$ while the losses are important for $z < z_{n_{max}}$ ($|\boldsymbol{j}_i^{'}|$ is comparable to its value at the chamber exit). Moreover, it is observed that $|\boldsymbol{j}_i^{'}|$ is relevant at the chamber back surface as well. One could know the importance of these losses by comparing their areas with the chamber exit area. For the back surface the ratio is 1, and for the portion of lateral wall up to $z_{n_{max}}$ the area is 6.4 times larger, and thus it is the main contribution for the losses.

- Subplot (h) illustrates the electron temperature. In regions of strong magnetization, the isolines of T_e follows the magnetic field lines due to the high heat conductivity along them.[19,20] T_e is below 3.5eV in most of the chamber, which results in important losses in excitation of neutrals. However, it is maximum (up to 6.8eV) for the field lines close to the lateral wall. The explanation for this behaviour is, first, there are important power deposition [subplot (g)] on those lines and, second, the low plasma density in that region due to confinement.

- The tendency of the electric potential [subplot (a)] is similar to that for n_e since an approximate Boltzmann-type relation exits between them.[15] There is an interesting feature near $(z, r) = (3.5, 0.75)$ cm: ϕ presents a bump, it increases with r and then it decays toward the wall; this is happens in strongly magnetized plasma, and the effect tries to regulate the flow of ions reaching the wall so that it equalizes the one for electrons.[29,30]

- Subplot (d) shows the ion longitudinal velocity. The trajectory of the ions follows the profile of ϕ and their acceleration in the plume (magnetic nozzle) is observed, which produces the thrust.

- Subplot (f) and (i) show the electron current density, the longitudinal component and the azimuthal one, respectively. Subplot (f) suggests that $\boldsymbol{j}_e^{'}$ is similar to $\boldsymbol{j}_i^{'}$ but not completely equal. Thus, local longitudinal electric currents are generated despite the free current condition downstream, something also observed in previous works.[14,15] Subplot (i) illustrates large azimuthal currents, these currents are responsible for the magnetic confinement[30] inside the chamber and for the generation of thrust in the plume.[31]

- The wave solution [subplots (g), (j), (k) and (l)] shows that, for the given plasma density and magnetic field profiles, the thruster falls in an operation regime where only the right hand polarized wave (whistler wave) propagates, being the left hand polarized mode evanescence. Looking at the fields, two characteristic wave-forms are identified, note that these are stationary wave patterns formed due to reflections in the metallic walls (boundary conditions of the W-module). In the upper right part of the plasma domain and visible in the three components of the field, the so called Trivelpiece-Gould (TG) mode appears. This electrostatic wave propagates perpendicular to the magnetic field lines, and is highly damped near the plasma boundary. On the other hand, close to the axis, longer wave lengths are observed in the azimuthal field, which correspond to the Helicon mode and propagate parallel to the applied magnetic field.

  Therefore, it is possible to classify the present propagation into the Double Wave Regime (DWR).[26] However, observe that both waves are indeed the same RHP wave, with high perpendicular wave number ($k_\perp$) and low $k_\perp$, respectively. As studied by Tian, Ahedo and Navarro,[32] this regime exists for $2\omega/\omega_{ce} < k_\parallel d_e < \sqrt{1/\left(\omega_{ce}/\omega - 1\right)}$, where $k_\parallel$ is the wavenumber in the direction parallel to the magnetic field.

C. Performances

Table 2 contains the performances of the thruster. In this table η_u and η_{prod} are the propellant utilization and production efficiency respectively, which are defined as

$$\eta_u = \frac{\dot{m}_{i,W3}}{\dot{m}} \text{ and } \eta_{prod} = \frac{\dot{m}_{i,W3}}{\dot{m}_{i,total}},$$

where $\dot{m}_{i,W3}$ is the ion mass flow through surface W3 and $\dot{m}_{i,total}$ through all the surfaces W1+W2+W3. The terms ϵ_{wall}, ϵ_{inel} and η_{ene} comes from the power balance, under steady conditions the total energy equation for all the species integrated over the whole domain yields

$$P_a = P_{wall} + P_{W3} + P_{ion} + P_{exc}.$$

Here P_{wall} is the total energy flux of all species through W1+W2, and P_{W3} is the useful one through W3, and P_{ion} and P_{exc} are the power spent in ionization and excitation respectively. Now, ϵ_{wall}, ϵ_{inel} and η_{ene} are defined as

$$\epsilon_{wall} = \frac{P_{wall}}{P_a},\ \epsilon_{inel} = \frac{P_{ion} + P_{exc}}{P_a} \text{ and } \eta_{ene} = \frac{P_{W3}}{P_a}.$$

Then there is the plume efficiency, η_{plu}, that measures the performance of the magnetic nozzle, defined as ratio between the axial and total ion energy flows through W3. Finally, F correspond to the thrust generated, and η_F is the thrust efficiency defined as

$$\eta_F = \frac{F^2}{2\dot{m}P_a},$$

and which can be estimated from the partial efficiencies as $\eta_F \approx \eta_u\eta_{ene}\eta_{plu}$.

In the table it is seen that the propellant utilization η_u is a 81%, which means a good ionization process, something already suggested by the previous analysis on the n_n-2D map. However, the production efficiency η_{prod} is only a 13%, and the plasma flow through W3 is small compare with the flow lost through the walls. Indeed, the ratio $\eta_u/\eta_{prod} = 6.23$ indicates that the propellant is ionized about 6 times. This is mainly due the recombination at that portion of the lateral wall up to $z_{n_{max}}$, as seen when discussing Fig. 5 (e). In order to mitigate this problem, one could set a magnetic topology that is more aligned with the lateral wall near that region and with a higher strength. Another solution could be just to move the back surface forward until z_{max}.

Looking at the power balance, η_{ene} is only a 4%. The rest is lost in wall recombination (ϵ_{wall}=31%) and inelastic collisions (ϵ_{inel}=65%). Inside ϵ_{inel}, the excitation is a 46%, and it is the main sink of power. This problem with excitation is due to the temperature profile analyzed in Fig. 4 (h). The solution for this problem is to change the antenna operation, for which parametric analysis is needed, so that the power deposition is concentrated close to the axis.

The plume efficiency η_{plu} is a 87% with a plume divergence semi-angle of $\arccos\sqrt{\eta_{plu}} = 21°$. Thus, the magnetic nozzle is operating properly. Despite that, due to the inefficiencies in the plasma generation inside the chamber the overall efficiency η_F is only a 1.9%.

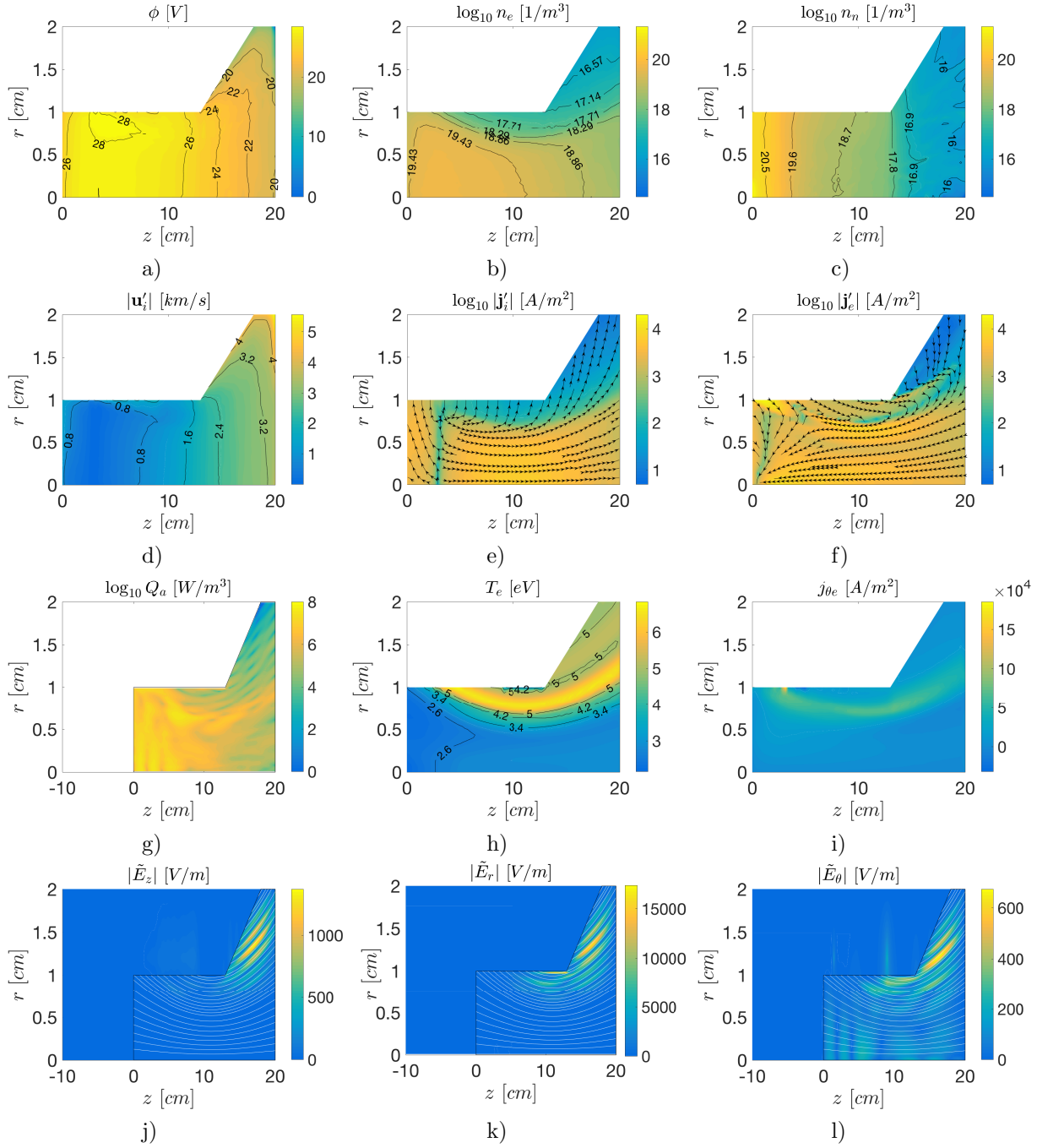

Figure 5. 2D maps of the plasma properties.

F [mN]	η_u	η_{ene}	η_{plu}	η_F	η_{prod}	ϵ_{inel}	ϵ_{wall}
3.2	0.81	0.04	0.87	0.019	0.13	0.65=0.46 + 0.19	0.31

Table 2. Performance indicators. The two terms in the sums of the the column ϵ_{inel} are the contributions of excitation and ionization (from left to the right).

V. Conclusions

A 2D asymmetric code for full plasma discharge simulations in HPTs has been introduced. This code has a block for the plasma transport, which follows a hybrid approach (fluid electrons and particles for heavy species). The main challenge of this approach is the numerical treatment for the anisotropic character of the magnetized electron fluid. Novel numerical advances in relation to the E-module have been briefly explained and described here. In order to handle the anisotropy, a MFAM mesh is considered and FDM is used for gradient reconstruction to minimize numerical diffusion. The use of a MFAM results in highly irregular cells close to the boundaries, and where complex algorithms based WLSM need to be applied to obtain the plasma properties. Coupled to the plasma transport block, there is a separate module that updates the power deposition map. The plasma-wave interaction physics is also complex to reproduce, and the development of a model that assumes a cold plasma and which is based on a frequency domain Finite Difference method has been detailed as well.

The code has been used to simulate a particular HPT thruster. Important conclusions have been obtained in relation to its design parameters such as its magnetic topology, chamber length, and antenna operation. These conclusions could help in the improvement of its performances. Moreover, as this thruster is quite similar to the prototype HPT05, it is clear the potential direct application the code has for a real case.

Acknowledgments

The authors acknowledge the financial support of Airbus Defence and Space to these research activities (Contract CW240050).

References

[1]T. Ziemba, P. Euripides, J. Slough, R. Winglee, L. Giersch, J. Carscadden, T. Schnackenberg, and S. Isley. Plasma characteristics of a high power helicon discharge. *Plasma Sources Science and Technology*, 15:517, 2006.

[2]D. Pavarin, F. Ferri, M. Manente, D. Curreli, Y. Guclu, D. Melazzi, D. Rondini, S. Suman, J. Carlsson, C. Bramanti, E. Ahedo, V. Lancellotti, K. Katsonis, and G. Markelov. Design of 50W helicon plasma thruster. In *31th International Electric Propulsion Conference*, IEPC 2009-205, 2009.

[3]E. Ahedo. Plasma dynamics in a helicon thruster. In *Proceedings of EUCASS 2011, 4-8 July 2011, Saint Petersburg, Russia*, paper 118, 2011.

[4]Y. Zhang, C. Charles, and R. Boswell. Characterization of an annular helicon plasma source powered by an outer or inner rf antenna. *Plasma Sources Science and Technology*, 25(1):015007, 2015.

[5]J Navarro-Cavallé, M Wijnen, P Fajardo, and E Ahedo. Experimental characterization of a 1 kw helicon plasma thruster. *Vacuum*, 149:69–73, 2018.

[6]J. Navarro-Cavallé, M. Wijnen, P. Fajardo, E. Ahedo, V. Gómez, A. Giménez, and M. Ruiz. Development and characterization of the helicon plasma thruster prototype hpt-03. In 36^{th} *International Electric Propulsion Conference*, number IEPC-2019-596, Vienna, Austria, 2019. Electric Rocket Propulsion Society.

[7]K. Takahashi. Helicon-type radiofrequency plasma thrusters and magnetic plasma nozzles. *Reviews of Modern Plasma Physics*, 3:3, 2019.

[8]E. Ahedo and J. Navarro-Cavallé. Helicon thruster plasma modeling: Two-dimensional fluid-dynamics and propulsive performances. *Physics of Plasmas*, 20(4):043512, 2013.

[9]T. Lafleur. Helicon plasma thruster discharge model. *Physics of Plasmas*, 21(4):043507, 2014.

[10]A. Domínguez, D. Pérez-Grande, P. Fajardo, and E. Ahedo. Nomads: Development of a versatile plasma discharge simulation platform for electric propulsion. In *Space Propulsion Conference 2016*, number paper 2016-3124869, Rome, Italy, May 2-6, 2016. Association Aéronautique et Astronautique de France.

[11]D. Pérez-Grande, J. Zhou, A. Domínguez-Vázquez, P. Fajardo, and E. Ahedo. Development updates for a two-dimensional axisymmetric hybrid code for plasma thruster discharges. In 35^{th} *International Electric Propulsion Conference*, number IEPC-2017-201, Atlanta, GA, 2017. Electric Rocket Propulsion Society.

[12]D. Pérez-Grande. *Fluid modeling and simulation of the electron population in Hall effect thrusters with complex magnetic topologies*. PhD thesis, Universidad Carlos III de Madrid, Leganés, Spain, 2018.

[13]Adrián Domínguez-Vázquez. *Axisymmetric simulaton codes for Hall effect thrusters and plasma plumes*. PhD thesis, Universidad Carlos III de Madrid, Leganés, Spain, To be defended, 2019.

[14]J. Zhou, A. Domínguez-Vázquez, D. Pérez-Grande, P. Fajardo, and E. Ahedo. An axisymmetric hybrid model for the plasma transport in a helicon plasma thruster. In *Space Propulsion Conference 2018*, number 00308, Seville, Spain, 2018. Association Aéronautique et Astronautique de France.

[15]J. Zhou, D. Pérez-Grande, P. Fajardo, and E. Ahedo. Numerical treatment of a magnetized electron fluid within an electromagnetic plasma thruster code. *Submitted to PSST*, 2019.

[16]Bin Tian, E. Ahedo, and Mario Merino. Development and validation of a 2D wave-plasma code for helicon plasma

thrusters. In *Space Propulsion Conference 2016*, page 3124913, Rome, Italy, 2016. Association Aéronautique et Astronautique de France.

[17]Bin Tian, Mario Merino, and E. Ahedo. Two-dimensional plasma-wave interaction in an helicon plasma thruster with magnetic nozzle. *Plasma Sources Science and Technology*, 27(11):114003, 2018.

[18]E. Ahedo and V. de Pablo. Combined effects of electron partial thermalization and secondary emission in Hall thruster discharges. *Physics of Plasmas*, 14:083501, 2007.

[19]F.I. Parra, E. Ahedo, J.M. Fife, and M. Martínez-Sánchez. A two-dimensional hybrid model of the Hall thruster discharge. *Journal of Applied Physics*, 100(2):023304, 2006.

[20]D. Escobar and E. Ahedo. Two-dimensional electron model for a hybrid code of a two-stage Hall thruster. *IEEE Transactions on Plasma Science*, 36:2043–2057, 2008.

[21]E. Shima, K. Kitamura, and T. Haga. Green-gauss/weighted-least-squares hybrid gradient reconstruction for arbitrary polyhedra unstructured grids. *AIAA Journal*, 51(11):2740 – 2747, 2013.

[22]E. Sozer, C. Brehm, and C.C. Kiris. Gradient calculation methods on arbitrary polyhedral unstructured meshes for cell-centered cfd solvers. In *52nd Aerospace Sciences Meeting*, National Harbor, Maryland, US, 2014.

[23]J.A. Bittencourt. *Fundamentals of plasma physics*. Springer, Berlin, Germany, 2013.

[24]Thomas H Stix. *Waves in plasmas*. Springer Science & Business Media, 1992.

[25]Jian-Ming Jin and Douglas J Riley. *Finite element analysis of antennas and arrays*. John Wiley & Sons, 2009.

[26]Bin Tian. *Modeling of physical processes in radio-frequency plasma thrusters*. PhD thesis, 2017.

[27]G. Chen, A.V. Arefiev, R.D. Bengtson, B.N. Breizman, C.A. Lee, and L.L. Raja. Resonant power absorption in helicon plasma sources. *Physics of Plasmas*, 13:123507, 2006.

[28]IV Kamenski and GG Borg. An evaluation of different antenna designs for helicon wave excitation in a cylindrical plasma source. *Physics of Plasmas*, 3:4396, 1996.

[29]L. Tonks. Theory of magnetic effects in the plasma of an arc. *Physical Review*, 56(4):360–373, 1939.

[30]E. Ahedo. Parametric analysis of a magnetized cylindrical plasma. *Physics of Plasmas*, 16(11):113503, 2009.

[31]E. Ahedo and Mario Merino. Two-dimensional supersonic plasma acceleration in a magnetic nozzle. *Physics of Plasmas*, 17(7):073501, 2010.

[32]Bin Tian, Eduardo Ahedo, and Jaume Navarro. Investigation of plasma-wave interaction in helicon antenna thrusters. In *50th AIAA/ASME/SAE/ASEE Joint Propulsion Conference*, 2014.